ChemPubSoc Europe

DOI: 10.1002/cplu.201500053

CHEMPLUSCHEM Full Papers

Reduced Graphene Oxide Composite with Oxidizable Manganese/Cobalt Mixed Oxide for *p*-Cresol Oxidation by Using Molecular Oxygen

Ajay Jha,[a] Sagar H. Patil,[b] Bhanu P. Solanki,[a] Ana P. C. Ribeiro,[c] Carlos A. N. Castro,[c] Kashinath R. Patil,[b] Alberto Coronas,[d] and Chandrashekhar V. Rode*[a]

A composite of graphene oxide (GO) with mixed oxide (MnCo) was prepared by using a solvothermal method. During the synthesis, both the reduction of GO and growth of metal oxides took place simultaneously. The as-prepared composite material was highly selective for the liquid-phase oxidation of *p*-cresol to form *p*-hydroxybenzaldehyde in 71% yield within 1 h. The composite material was characterised by SEM, X-ray photoelectron spectroscopy, high-resolution TEM and cyclic voltammetry (CV). A CV study revealed that the increase in the redox potential of the mixed oxide after being supported on GO, led to its higher activity of the catalyst for the oxidation reaction. The stability of the catalyst under the reaction conditions was studied by its successful reuse in three cycles.

Introduction

Side-chain oxidation of *p*-cresol is a very challenging reaction from both fundamental and application points of view because the distribution of oxidation products, such as *p*-hydroxybenzyl alcohol (PHBAlc), *p*-hydroxybenzaldehyde (PHBAld) and *p*-hydroxybenzoic acid (PHBAcid), is strongly influenced by the catalyst and reaction conditions. All these products of *p*-cresol oxidation (Scheme 1) have versatile applications in industrial and pharmaceutical sectors.[1,2] Industrially, PHBAld is synthesised by side-chain chlorination of *p*-cresol and subsequent saponification of the resulting dichloromethyl group.[3] Sharma and Chandalia reported the oxidation of *p*-cresol in methanol by using cobaltous chloride in the presence of NaOH to give 90% conversion with 59% selectivity to PHBAld.[4] Major drawbacks of this route are the employment and generation of chemicals that are detrimental to health and the environment and longer reaction times. These can be overcome by using a suitable heterogeneous catalyst, which clearly has advantages of ease of separation from the reaction mixture and easy handling. Nevertheless, disadvantages include limited activity and selectivity because of the solid matrix, which limits mobility and accessibility of the active sites.[5] In this respect, the dispersion of metal oxide nanoparticles (NPs) on graphene sheets potentially provides a novel way to develop more efficient catalysts for oxidation reactions.[6] The use of graphene-based composite materials, owing to their unique structure and extraordinary properties, is known for various other applications, such as electrocatalysts, electrodes and sensors; however, their exploration in catalysis is limited.

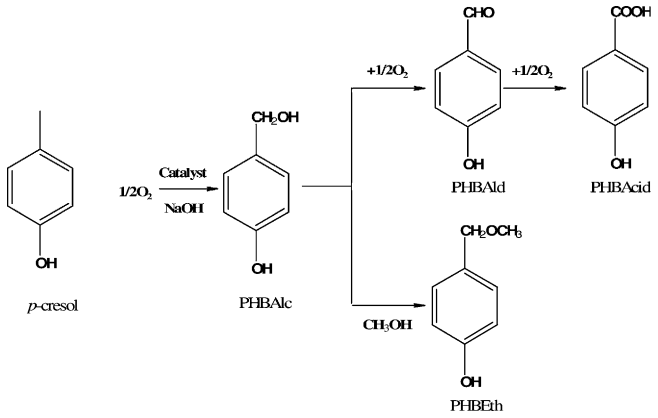

Scheme 1. Reaction products of *p*-cresol oxidation.

Herein, a catalyst based on a graphene oxide (GO) composite is reported for the first time for the liquid-phase oxidation of *p*-cresol. The surface of GO hosts oxygen-containing functional groups, such as hydroxyl (–OH) and epoxide groups located on the basal planes, and carbonyl (>C=O) and carboxyl groups (–COOH) located at the edges of GO.[7] These function-

[a] Dr. A. Jha, B. P. Solanki, Dr. C. V. Rode
Chemical Engineering and Process Development
CSIR-National Chemical Laboratory
Pune 411008 (India)
E-mail: c.v.rode@ncl.res.in

[b] S. H. Patil, Dr. K. R. Patil
Centre for Materials Characterization
CSIR-National Chemical Laboratory
Pune 411008 (India)

[c] Dr. A. P. C. Ribeiro, Prof. C. A. N. Castro
Centro de Química Estrutural
Faculdade de Ciências da Universidade de Lisboa
Campo Grande, 1749-016 Lisboa (Portugal)

[d] Prof. A. Coronas
Department of Mechanical Engineering
Universitat Rovira I Virgili, 43007 Tarragona (Spain)

Supporting information for this article is available on the WWW under http://dx.doi.org/10.1002/cplu.201500053.

al groups facilitate the anchoring of semiconductors, metal NPs and so forth, which are useful for performing redox reactions and open up new opportunities for designing novel catalysts. GO is an excellent precursor for graphene synthesis, through either chemical or thermal reduction processes. A number of chemical reductants have been studied for the reduction of GO to form graphene/metal NPs composites, for example, hydrazine and its derivatives.[8,9] However, these reductants are highly toxic and explosive, which limit their usage on a larger scale. Therefore, we used ethylene glycol, which is safe and environmentally friendly, as a reducing agent.[10] Although cobalt is an excellent catalyst for activation of the relatively inert C–H bond in oxidation reactions, the additional incorporation of manganese is known to improve the overall oxidation activity and, more particularly, influence the product distribution owing to the formation of efficient redox couple between cobalt and manganese.[11,12] The combination of these two metal oxides (MnOx and CoOx) has been reported previously for the oxidation of volatile organic compounds.[13] Recently, our group has also reported manganese-doped cobalt oxide as a highly active catalyst for the selective liquid-phase aerobic oxidation of vanillyl alcohol under base-free conditions.[14] Inspired by these results, and considering the catalytically useful characteristics of reduced graphene oxide (r-GO), we attempted to develop a composite of r-GO with mixed metal oxides (MnCo) as a novel heterogeneous catalyst. This is reported, for the first time, for the selective oxidation of *p*-cresol to form PHBAld. The activity of the catalyst was correlated with its physicochemical characterisation data obtained from various techniques.

Results and Discussion

The powder XRD pattern of MnCo mixed oxide (MO) in Figure 1a shows diffraction peaks of three different spinel oxides. The peaks at $2\theta = 33.1$ (103), 39.6 (004) and 54.6° (312) correspond to the tetragonal phase of $CoMn_2O_4$ (JCPDS no.77-0471). However, peaks at $2\theta = 24.5$ (101) and 41.7° (103) were attributed to the tetragonal phase of Mn_3O_4 (JCPDS no. 24-0734), and those at $2\theta = 19$ (111), 31.1 (220), 36.6 (311), 44.7 (400), 59.1 (511) and 65.2° (440), were ascribed to the cubic phase of Co_3O_4 (JCPDS no. 74-1657). The XRD pattern of the reduced graphene oxide composite with MnCo MO (r-GO–MnCo) in Figure 1b shows the intact diffraction peaks of spinel oxides of $CoMn_2O_4$, Co_3O_4 and Mn_3O_4, without any change in the metal oxide phases after being supported on r-GO. However, the peak intensities reduced owing to the decrease in crystallite sizes. The crystallite size calculated by considering the sharp peak of (311) was found to be 10 nm in the case of MnCo MO, whereas it was 8 nm for r-GO–MnCo.

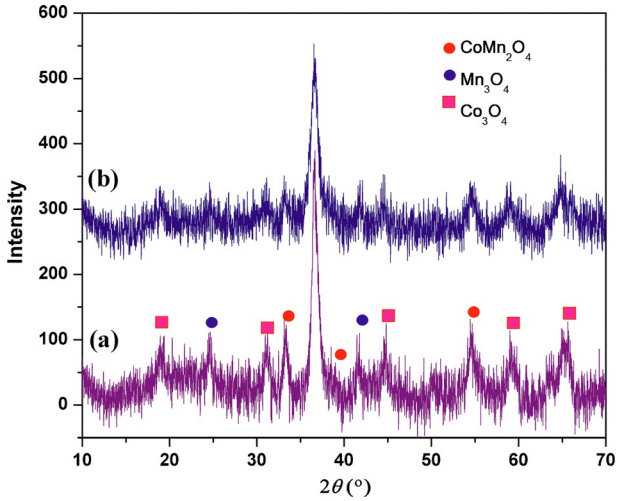

Figure 1. XRD patterns of a) MnCo MO and b) r-GO–MnCo.

Figure 2a shows a SEM image of the GO powder, and indicates that the surfaces of the GO sheets have a wrinkled paper-like morphology, which may be due to the oxidation pre-treatment.[15] A TEM image of the r-GO sample exhibited a thin, sheet-like structure with good separation and a fairly large area (Figure S1). The few dark ripples that appeared on the surface could arise from the scrolling and crumpling of nanolayers during the formation of sheets. Figure 2b,c gives HR-TEM images of the r-GO–MnCo composite, which clearly show that the morphology of the MnCo NPs does not change after the formation of a composite with r-GO because the bare mixed metal oxide also has the same morphology (Figure S1), leading to the uniform distribution of NPs on GO sheets with high density. The r-GO–MnCo nanocomposite showed the mixed morphology of spindle and spherical shapes. The spindle-shaped particles were 6 nm in diameter with a length of 25 nm, whereas the spherical particles had a diameter of 8 nm. The lattice fringe patterns of the r-GO–MnCo catalyst in Fig-

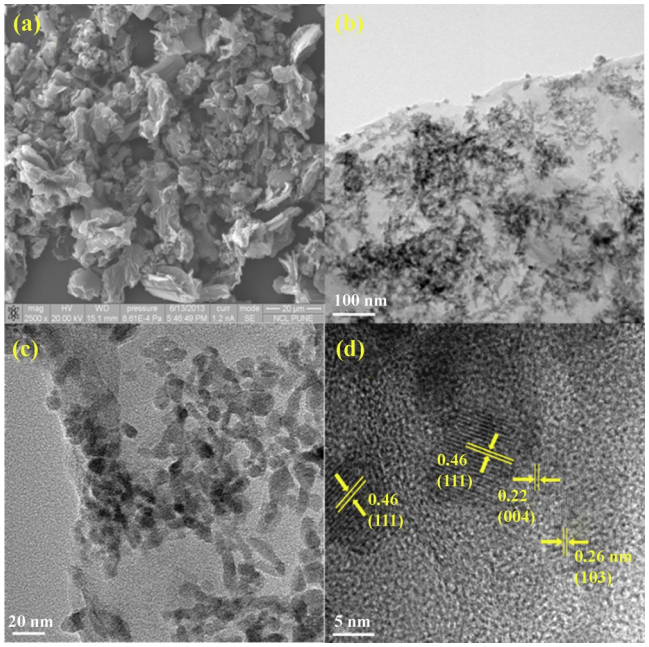

Figure 2. a) SEM image of the GO powder. b) and c) High-resolution (HR) TEM images of the r-GO–MnCo catalyst. d) Lattice fringe pattern of r-GO–MnCo.

ure 2d showed the dominant exposed planes as (111) in the r-GO–MnCo nanocomposite with a lattice spacing of 0.46 nm, which was related to spinel Co_3O_4. The other exposed planes were (103) and (004) with lattice spacings of 0.26 and 0.22 nm, respectively, which were related to the mixed spinel phase of $CoMn_2O_4$.

X-ray photoelectron spectroscopy (XPS) results for the C 1s of GO and r-GO–MnCo are shown in Figures 3a,b. The C 1s XPS region was deconvoluted into four peaks that corresponded to four different bonding environments of carbon, including sp^2-carbon atoms in aromatic rings ((284.6±0.2) eV), namely, carbon atoms bonded to hydroxy and epoxy (C–OH, (286.5±0.1) eV), carbonyl (>C=O, (287±0.3) eV) and carboxyl groups (COOH, (287.9±0.3) eV).[16] Compared with GO, the XPS results for C 1s in r-GO–MnCo (Figure 3b) showed a reduction in the intensity of oxygen-containing carbon species. At the same time, we observed that there was also a decrease in the total relative area of the peaks corresponding to these functional groups. This result confirmed that the functional groups containing oxygen were reduced during synthesis of the catalyst in the presence of ethylene glycol.

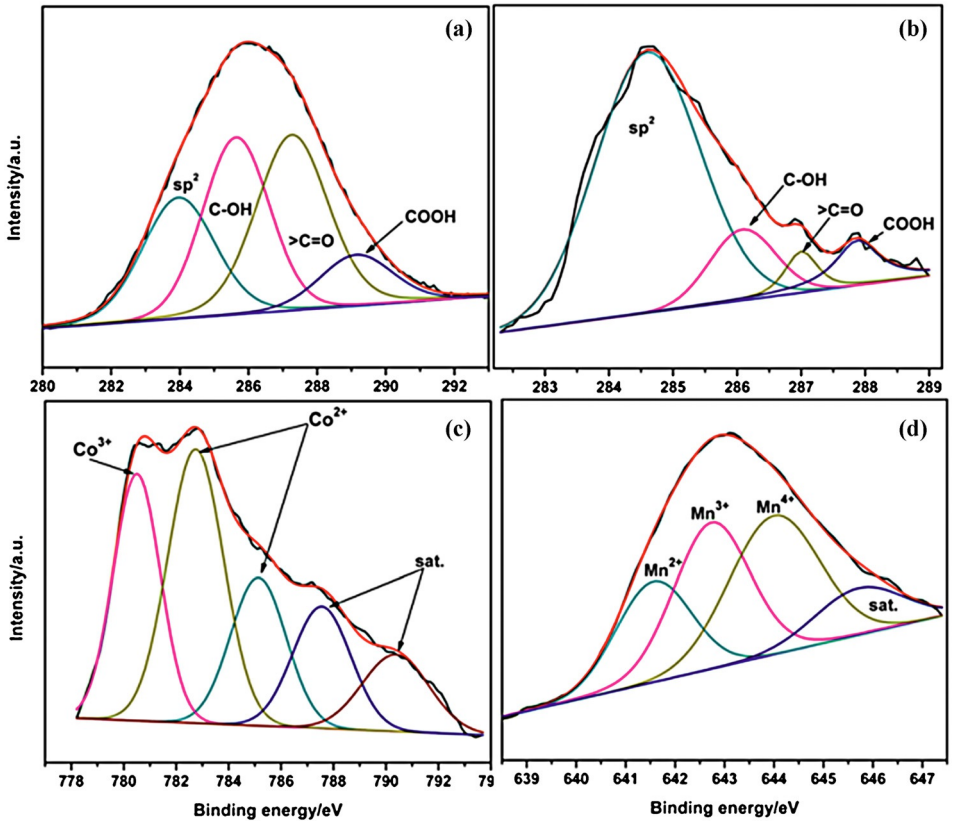

Figure 3. XPS results for a) C 1s of GO, b) C 1s of r-GO–MnCo, c) Co $2p_{3/2}$ and d) Mn $2p_{3/2}$ of the r-GO–MnCo nanocomposite.

In the r-GO–MnCo nanocomposite, the peak owing to Co $2p_{3/2}$ was unsymmetrical and broad; this could be fitted satisfactorily to three principal and two satellite peaks after deconvolution (Figure 3c). The peak at 780.5 eV was assigned to Co^{3+} of Co_2O_3, whereas the peak at 782.8 eV was assigned to Co^{2+} of $CoMn_2O_4$. The formation of $CoMn_2O_4$ was also confirmed by XRD and HR-TEM results. Another peak at 785.2 eV was also present owing to Co^{2+}, but this came from spinel Co_3O_4. The appearance of two satellite peaks at 787.4 and 790.2 eV was indicative of Co^{2+} in spinel $CoMn_2O_4$ and Co_3O_4, respectively. All peaks showed a positive shift towards higher binding energy (BE) relative to the bare mixed metal oxides (MnCo MO; Figure S2). The change in the electronic states of the metals to higher valence states confirmed the formation of the r-GO–MnCo nanocomposite. This trend can be interpreted as delocalisation of electrons owing to dπ–pπ interactions between metal d orbitals and the carbon p orbital of r-GO, as a result of strong interactions between r-GO and the metal oxide.[17]

The XPS spectrum of the r-GO–MnCo nanocomposite also showed a broad peak of Mn $2p_{3/2}$, which could be fitted satisfactorily to three major peaks and a satellite peak after deconvolution, as shown in Figure 3d. The peaks at 641.5, 642.7 and 643.9 eV corresponded to Mn^{2+}, Mn^{3+} and Mn^{4+}, respectively, whereas the small peak at 645.7 eV was assigned to the satellite of Mn^{4+}. The existence of Mn^{3+}, Mn^{2+} and Mn^{4+} species was due to the formation of $CoMn_2O_4$ and Mn_3O_4 spinel oxides, the presence of which was also confirmed by XRD diffraction peaks at $2\theta = 33.1$ (103) and 24.5° (101), respectively. However, the presence of Mn^{4+} indicates the possibility of the presence of MnO_2, which we did not observe in the XRD results owing to peak broadening. Similar to cobalt, a shift in the BE of manganese was also observed; this could be due to extremely effective delocalised donor–acceptor interactions with the π system of r-GO (Figure S3).

The manner in which oxygen is bound to metals in the r-GO–MnCo nanocomposite can be determined by the XPS of oxygen. Deconvolution of the O 1s spectrum of pure GO produced three peaks at approximately 530.1, 531.8 and 532.8 eV. These peaks have been assigned to >C=O, –COOH and –OH residual oxygen-containing groups, respectively, bound with carbon atoms in GO (Figure S4).[18] However, the deconvolution of O 1s spectra in the case of metal oxide composites with r-GO yielded four peaks. The peaks at lower BE values of 529.5–530.5 eV could be assigned to oxygen species involved in metal oxide bonds in the composite and must therefore correspond to Co–O and Mn–O, respectively.[19] However, peaks at

higher binding energies in the case of metal composites were assigned to >C=O, –COOH and –OH residual oxygen-containing groups, which helped to bind metals on the surface of partially reduced GO.

The active sites present in the r-GO–MnCo catalyst could be approximately estimated by cyclic voltammetry (CV). CV measurements were performed at a scan rate of 100 mV s^{-1} over the potential range of 0–0.8 V in a 0.5 M solution of H_2SO_4 by using a glassy carbon electrode. Figure 4 shows the plots of

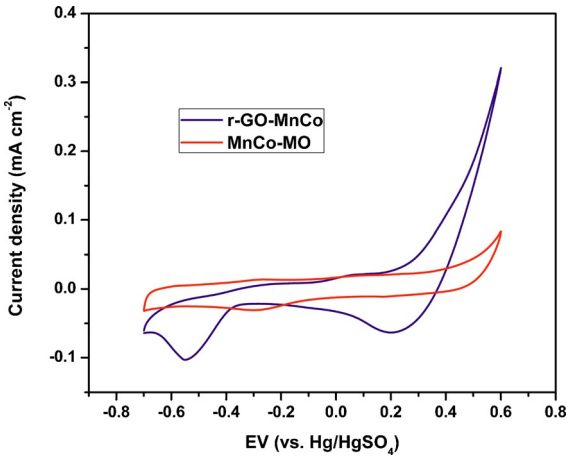

Figure 4. CV curves of MnCo MO and the r-GO–MnCo nanocomposite.

current density versus potential for the MnCo MO and r-GO–MnCo nanocomposite. It is clear that the r-GO–MnCo nanocomposite presents the largest integrated area, compared with bare MnCo MO, which indicates that the redox potential of the nanocomposite has been significantly increased owing to the addition of GO.[20] The enhancement in redox potential of the r-GO–MnCo nanocomposite material can be ascribed to 1) the larger specific surface area (154 m^2 g^{-1}) than that of bare MnCo MO (85 m^2 g^{-1}), 2) the smaller particle size (8 nm) and 3) the synergistic effect between the r-GO and MnCo NPs. Therefore, a decrease in particle size increased the active surface that took part in the redox reactions.[17] Both samples (MnCo MO and r-GO–MnCo nanocomposite) showed clearly the presence of oxidation and reduction peaks. However, the r-GO–MnCo nanocomposite showed two very sharp reduction peaks: one at higher potential value (0.2 V), which could be assigned to the reduction of Mn^{3+} to Mn^{2+}, and the second one at a lower potential value (−0.55 V), which could be assigned for the further reduction of Mn^{2+} and Co^{2+} to metallic Mn and Co, respectively.[21] Compared with the bare MnCo MO, a substantial negative shift (from −0.28 to −0.55 V) of the cathodic peak was observed for r-GO–MnCo, which indicated increased electron density of the Co^{2+} and Mn^{2+} species.[22] The reduction peak indicates the reduction ability of oxygen; hence, as the potential value shifted to more and more negative values, the oxygen reduction ability increased, which led to the higher oxidation ability of r-GO–MnCo for *p*-cresol to form PHBAld. A similar study was reported for Mn_3O_4 composite with multiwalled carbon nanotubes (MWCNTs).[23]

Catalyst activity

The performance of different catalysts for *p*-cresol oxidation was studied under the same reaction conditions (Table 1). A blank run without catalyst gave only 6% yield of product with higher selectivity to PHBAcid (60%). However, in the absence of NaOH, no reaction took place. It is known that NaOH forms the phenolate ion, which is the active species for the oxidation reaction.[14] A systematic study on the effect of NaOH concentration was also reported, and showed that a minimum ratio of NaOH/*p*-cresol was required, below which the selectivity to PHBAld could be as low as 11% owing to the oxidative dimerisation of *p*-cresol to give the dihydroxy diphenyl compound.[24] Therefore, it was concluded that NaOH was essential for *p*-cresol oxidation. Table 1 also shows that monometallic oxide catalysts exhibited lower activity than the bimetallic catalysts. Interestingly, the r-GO–Co catalyst was highly selective for PHBAld formation, whereas the r-GO–Mn catalyst was highly selective for PHBAlc formation.

Table 1. Catalyst screening for *p*-cresol oxidation.

Catalysts	Yield [%]	Selectivity [%]			
		PHBAlc	PHBAld	PHBAcid	PHBEth
WO[a]	6	2	38	60	–
r-GO–Co	20	–	89	10	1
r-GO–Mn	28	100	–	–	–
MnCo (1:1)	42	1	95	3	1
r-GO–MnCo (1:1)	71	–	96	3	1
r-GO–MnCo (1:2)	57	–	97	2	1
r-GO–MnCo (2:1)	60	1	95	3	1
r-GO–MnCo (1:1)	NR[b]	–	–	–	–
MnCo (1:1)/SiO_2	9	–	93	6	1
MnCo (1:1)/Al_2O_3	31	–	93	6	1

[a] WO = without catalyst. [b] NR = no reaction (reaction performed in the absence of base).

The addition of manganese to the cobalt oxide led to a complete change in both the selectivity pattern and catalyst activity. The mixed metal oxides (MnCo MO) exhibited higher catalytic activity than that of the monometallic catalyst, regardless of whether cobalt or manganese alone was used as the active phase. The higher activity of the mixed metal oxides was due to the cooperative effect between the metals towards an increment in the mobility of oxygen as well as stabilising the more active species. The redox cycles, which also permit reactivation of the catalyst, are also favoured. Manganese, in synergism with cobalt oxide, improves the superficial oxygen availability at the catalyst surface, which is attributed to the high oxygen storage capacity of manganese.[25] The r-GO–MnCo catalyst showed a higher activity (71% product yield) than those of bare mixed metal oxide (42% product yield) without affecting the selectivity pattern. This observation suggests that the GO-doped catalyst was efficient for sustainable redox couple formation ($M^{n+} \leftrightarrow M^{(n+1)+}$). The change in the oxidising ability of the catalyst by increasing the electron density on to the metal oxide through delocalisation of electrons through π–π interac-

tions of r-GO was supported by results from CV analysis. The GO-based catalysts also provide anchoring sites for aromatic substrates through π–π interactions; this increases the probability of adsorption of a substrate on the catalyst surface, leading to a higher reaction rate. Furthermore, to reveal the importance of r-GO as a support, we performed the oxidation experiments with MnCo (1:1) catalysts supported on traditional supports, such as silica and alumina, and the results are also shown in Table 1. Both catalysts gave much lower activities than those for r-GO-supported MnCo MO catalysts.

In this study, all catalysts were prepared by varying the ratios of cobalt and manganese with a constant amount of GO (1%). The Mn/Co ratio in the catalysts was determined by energy-dispersive X-ray spectroscopy (EDS), the results of which were close to the calculated values (Figure S5). Among the screened catalysts, we observed that a 1:1 ratio of Co/Mn showed a higher catalytic activity (71% product yield) than those of GO–MnCo (1:2) and GO–MnCo (2:1), which gave product yields of 57 and 60%, respectively. Because the r-GO–MnCo (1:1) catalyst gave a better performance, further study on the optimisation of the reaction parameters was performed with this catalyst. Figure 5 shows the time course of the catalytic performances in

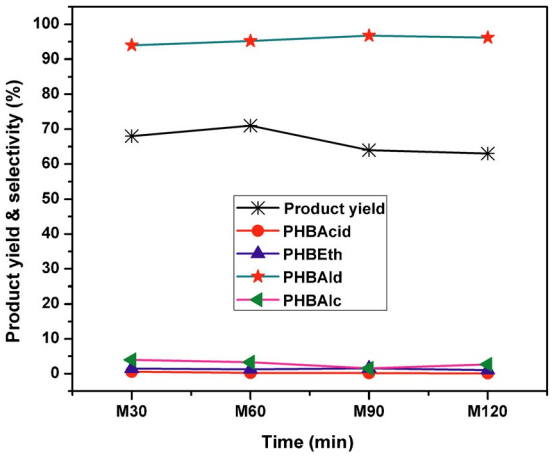

Figure 5. Effect of time on *p*-cresol oxidation. Reaction conditions: *p*-cresol (55.5 mmol), NaOH (155 mmol), r-GO–MnCo catalyst (0.2 g), 100 °C, methanol (50 mL), oxygen (2.7 bar).

p-cresol oxidation with r-GO–MnCo (1:1) catalyst under 2.7 bar of oxygen. The product yield increased from 68 to 71% by extending the reaction time from 30 to 60 min. Thereafter, a decrease in the product yield occurred from 71 to 60% in 2 h; this might be due to the formation of a tarry product, which was detected only after the reaction was continued for a longer reaction time (2 h). However, selectivity to PHBAlc, PHBAcid and PHBEth throughout the reaction remained only <4% and the selectivity for PHBAld was >96%.

The stability of the r-GO–MnCo catalyst for *p*-cresol oxidation was established by performing experiments to reuse the catalyst. Briefly, after the first oxidation run with fresh r-GO–

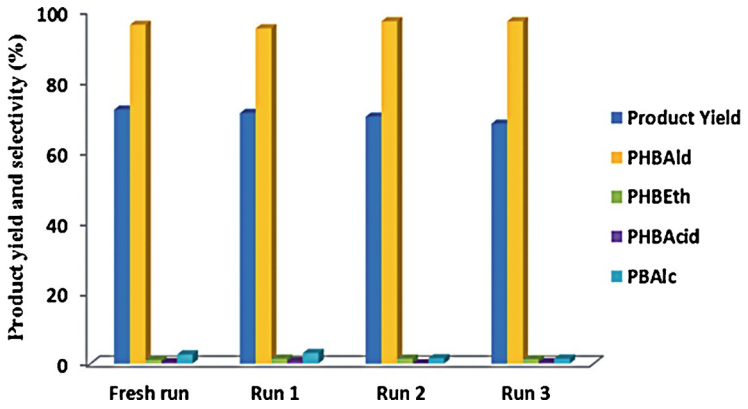

Figure 6. Recycling studies for the r-GO–MnCo catalyst. Reaction conditions: *p*-cresol (55.5 mmol), NaOH (155 mmol), r-GO–MnCo catalyst (0.1 g), 100 °C, methanol (50 mL), oxygen (2.7 bar), 1 h.

MnCo nanocomposite, the catalyst was filtered and washed several times with methanol, dried at 100 °C for 6 h, and reused for subsequent runs by adding fresh reactants. Figure 6 shows that the catalyst retained its activity, even after third cycle; this indicates the high efficiency of the r-GO–MnCo catalyst for the oxidation of *p*-cresol. To check the stability of the r-GO–MnCo catalyst, and verify that the reaction was truly heterogeneously catalysed, a leaching experiment was also performed. After 30 min of reaction, the catalyst was filtered and the reaction continued for another 30 min. The product yields measured before and after catalyst filtration were 68 and 66.5%, respectively, which confirmed that the reaction was heterogeneous and also that there was no metal leaching under these reaction conditions.

Conclusion

In the liquid-phase oxidation of *p*-cresol to form PHBAld, r-GO proved to be a highly efficient support for the mixed metal oxide (MnCo MO) catalyst. The structural characteristics of r-GO provided active sites for adsorbing *p*-cresol through π–π stacking interactions. In addition, the r-GO support caused charge transfer, which led to the enhancement in the redox potential of the MnCo MO. Both these factors led to the increased rate of oxidation to give a product yield of 71% with >96% selectivity to PHBAld in 1 h from *p*-cresol oxidation under mild reaction conditions.

Experimental Section

Preparation of GO and r-GO–MnCo nanocomposite

A modified Hummers' method was used to synthesise GO, in which graphite powder (1.0 g) was poured into a solution of $NaNO_3$ (0.5 g) in concentrated H_2SO_4 (30 mL) and cooled to 0 °C. $KMnO_4$ (3.0 g) was then added, during which the temperature of the mixture was maintained below 20 °C. Successively, the mixture was stirred at 35 °C for 1 h, and then diluted with deionised water (46 mL) by keeping the temperature at 85 °C and then increasing it to 100 °C for 30 min. Warm deionised water (140 mL) was then

added to the mixture, followed by the dropwise addition of a 50% aqueous solution of H_2O_2 (15 mL), and the solution was stirred for 30 min. The mixture was then centrifuged and washed with a 5% aqueous solution of HCl (1 L) to remove metal ions, followed by deionised water (1 L) to remove the acid. The resulting solid was dried in air for 12 h at 60 °C.

r-GO–MnCo nanocomposite was synthesised by a solvothermal method. In a typical synthesis, GO was dispersed into ethylene glycol (60 mL) and sonicated for 1 h, followed by the subsequent addition of aqueous NH_3 (1.6 mL), and stirred again for 1 h. Manganese and cobalt acetates were added in a 1:1 molar ratio and the solution was gradually heated to 160 °C. As the temperature reached 160 °C, a 0.3 M aqueous solution of Na_2CO_3 (200 mL) was added dropwise and the slurry was further aged for 2 h under a nitrogen atmosphere. The resulting product was filtered, thoroughly washed with distilled water until neutralisation, and dried overnight at 100 °C, then calcined at 350 °C for 4 h.

MnCo (1:1) oxide supported on SiO_2 and Al_2O_3 catalysts were obtained by a wet impregnation method. The synthesis involved dissolution of Mn and Co precursors into methanol (50 mL). After complete dissolution of the metal precursors, SiO_2/Al_2O_3 was added to the solution. The suspension was stirred for 6 h and then the solvent was removed in vacuo. The obtained solid product was dried at 100 °C for 12 h and then calcined at 350 °C for 4 h.

Catalyst characterisation

XRD patterns of the catalysts were recorded in the 2θ range of 10–80° (scan rate of 5.3° min^{-1}) on a PANalytical PXRD Model X-Pert PRO-1712 instrument by using Ni-filtered $Cu_{K\alpha}$ radiation (λ = 0.154 nm) as a source (current intensity, 30 mA and 40 kV) and an Xcelerator detector. The microscopic features of the GO were characterised by means of an Environ scanning electron microscope (E-SEM, Quanta 200 3D). The morphology and size of the as-prepared products were observed by HR-TEM (JEOL 2010F) at an acceleration voltage of 300 kV. The surface chemistry was analysed by using an X-ray photoelectron spectrometer (XPS, VG Micro Tech ESCA-3000). The chamber pressure was about 1×10^{-9} torr under the testing conditions. The surface area of the samples was obtained by the BET method.

Catalytic reactions

All catalytic oxidation reactions were performed in a 300 mL high-pressure Hastelloy reactor supplied by Parr Instruments Co. USA. The reactor was connected to an oxygen cylinder held at a pressure higher than that of the reactor. A Thermo Scientific HPLC model AS3000 liquid chromatograph equipped with a UV detector was used for analysis. HPLC analysis was performed on a 25 cm RP-18 column. The products and reactant were detected by using a UV detector at λ_{max} = 254 nm. Aqueous methanol (35%) was used as a mobile phase at a column temperature of 35 °C and a flow rate of 1 mL min^{-1}.

In a typical experiment, *p*-cresol (6.0 g), NaOH (6.2 g) and methanol (50 mL) were heated in a round-bottomed flask fitted with a reflux condenser until all NaOH dissolved completely. This reaction mixture was charged into a 300 mL Parr autoclave. Then, the catalyst (0.2 g) was added and the reaction mixture was heated to 373 K. After the desired temperature was attained, the reactor was pressurised with oxygen (2.7 bar). Then, the reaction was started by agitating at 1000 rpm. When the pressure decreased, the reactor was again filled with oxygen. This was continued for up to 2 h. The progress of the reaction was monitored by observing the pressure drop in the reservoir vessel as a function of time. After 2 h, the reactor was cooled to room temperature and excess oxygen gas was safely vented. The contents of the reactor were discharged and the final volume was recorded and the liquid samples were analysed by HPLC.

Acknowledgements

A.J. gratefully acknowledges the Council of Scientific and Industrial Research (CSIR, New Delhi) for the award of a senior research fellowship.

Keywords: cyclic voltammetry · graphene · oxidation · supported catalysts · transition metals

[1] H. V. Borgaonkar, B. C. Sampatraj, *J. Chem. Technol. Biotechnol.* **1984**, *34*, 107–112.
[2] V. S. Kshirsagar, A. C. Garade, K. R. Patil, R. K. Jha, C. V. Rode, *Ind. Eng. Chem. Res.* **2009**, *48*, 9423–9427.
[3] A. Thoer, G. Denis, M. Delmas, A. Gaset, *Synth. Commun.* **1988**, *18*, 2095–2101.
[4] S. N. Sharma, S. B. Chandalia, *J. Chem. Technol. Biotechnol.* **1990**, *49*, 141–153.
[5] M. Gruttadauria, F. Giacalone, R. Noto, *Green Chem.* **2013**, *15*, 2608–2618.
[6] B. F. Machadoab, P. Serp, *Catal. Sci. Technol.* **2012**, *2*, 54–75.
[7] V. Georgakilas, M. Otyepka, A. B. Bourlinos, V. Chandra, N. Kim, K. C. Kemp, P. Hobza, R. Zboril, K. S. Kim, *Chem. Rev.* **2012**, *112*, 6156–6214.
[8] S. Wang, X. Wang, S. P. Jiang, *Phys. Chem. Chem. Phys.* **2011**, *13*, 6883–6891.
[9] Y. Hu, H. Zhang, P. Wu, H. Zhang, B. Zhou, C. Cai, *Phys. Chem. Chem. Phys.* **2011**, *13*, 4083–4094.
[10] C. Xu, X. Wang, J. Zhu, *J. Phys. Chem. C* **2008**, *112*, 19841–19845.
[11] F. Wang, G. Yang, W. Zhang, W. Wu, J. Xu, *Chem. Commun.* **2003**, 1172–1173.
[12] D. A. Aguilera, A. Perez, R. Molina, S. Moreno, *Appl. Catal. B* **2011**, *104*, 144–150.
[13] Z. Y. Tian, P. H. Tchoua Ngamou, V. Vannier, K. K. Höinghaus, N. Bahlawane, *Appl. Catal. B* **2012**, *117–118*, 125–134.
[14] A. Jha, K. R. Patil, C. V. Rode, *ChemPlusChem* **2013**, *78*, 1384–1392.
[15] L. Zhang, L. Jiang, H. Yan, W. D. Wang, W. Wang, W. Song, Y. Guo, J. Wan, *J. Mater. Chem.* **2010**, *20*, 5462–5467.
[16] X. Huo, J. Liu, B. Wang, H. Zhang, Z. Yang, X. She, P. Xi, *J. Mater. Chem. A* **2013**, *1*, 651–656.
[17] J. Zhu, A. Holmen, D. Chen, *ChemCatChem* **2013**, *5*, 378–401.
[18] H. Karami, B. Kafi, S. N. Mortazavi, *Int. J. Electrochem. Sci.* **2009**, *4*, 414–424.
[19] Z. S. Wu, W. Ren, L. Wen, L. Gao, J. Zhao, Z. Chen, G. Zhou, F. Li, H. M. Cheng, *ACS Nano* **2010**, *4*, 3187–3194.
[20] C. Du, Z. Yao, Y. Chen, H. Bai, L. Li, *RSC Adv.* **2014**, *4*, 9133–9138.
[21] L. Wang, B. Liu, S. Ran, L. Wang, L. Gao, F. Qu, D. Chen, G. Shen, *J. Mater. Chem. A* **2013**, *1*, 2139–2143.
[22] J. Xu, P. Gao, T. S. Zhao, *Energy Environ. Sci.* **2012**, *5*, 5333–5339.
[23] M. Biswal, V. V. Dhas, V. R. Mate, A. Banerjee, P. Pachfule, K. L. Agrawal, S. B. Ogale, C. V. Rode, *J. Phys. Chem. C* **2011**, *115*, 15440–15448.
[24] C. V. Rode, M. V. Sonar, J. M. Nadgeri, R. V. Chaudhari, *Org. Process Res. Dev.* **2004**, *8*, 873–878.
[25] Q. Zhang, X. Liu, W. Fan, Y. Wang, *Appl. Catal. B* **2011**, *102*, 207–214.

Received: February 5, 2015
Revised: March 18, 2015
Published online on April 27, 2015